



Work hardening for powder bed fusion–laser beam (PBF-LB) AlSi10Mg alloy manufactured at different orientations and its application for Vickers hardness evaluation

George Crawford¹ · Ahmad Serjouei¹

Received: 15 November 2024 / Accepted: 28 April 2025
© The Author(s) 2025

Abstract

Powder bed fusion–laser beam (PBF-LB) is one of the additive manufacturing (AM) techniques that have grown in demand in recent years due to the ability to produce extremely lightweight, ultra-high-strength metals necessary for the aerospace industry. Aluminium alloys such as AlSi10Mg manufactured using PBF-LB exhibit anisotropic mechanical behaviour and variable plastic deformation characteristics, posing challenges for broader structural applications. This paper presents a comprehensive overview of the mechanical properties of AlSi10Mg, covering ultimate tensile stress (UTS), elongation at fracture, yield stress (YS), work hardening, hardening capacity, toughness, and hardness. Hollomon and Voce methods are used for approximating work hardening of PBF-LB AlSi10Mg printed at different orientations. Improved Hollomon and Voce approximations are presented using Levenberg–Marquardt (LM) least square method, and it is shown that improved Hollomon and Voce approximations show superior accuracy in predicting work hardening behaviour of the material compared to the original Hollomon and Voce approximations. A unique method of obtaining Vickers hardness of AM materials purely from tensile testing and use of work hardening, rather than direct hardness testing, is also presented, which potentially reduces the time and cost of hardness testing, especially in the absence of hardness testing facilities.

Keywords Work hardening · Additive manufacturing · Printing orientation · Vickers hardness

Abbreviations

AM	Additive manufacturing
AB	As-built
COD	Coefficient of determination
DIC	Digital image correlation
HT	Heat-treated
LM	Levenberg–Marquardt
OAT	One-at-a-time
PBF-LB	Powder bed fusion–laser beam
SD	Standard deviation
SHT	Solution heat-treated
UTS	Ultimate tensile stress
YS	Yield stress

1 Introduction

Powder bed fusion–laser beam (PBF-LB) has been utilised in many industries, including aerospace and automotive industries, due to its ability to produce complex geometries [1–4]. One of these alloys prominently produced via PBF-LB is AlSi10Mg, due to its great printability and weldability, as well as its high strength and lightweight structure [5]. PBF-LB AlSi10Mg is favoured over casting, due to the greater strength and work hardening capacities achieved compared to cast Al–Si alloys [6].

Work hardening, also known as strain hardening or cold working, is a mechanical phenomenon that occurs in materials when they are subjected to plastic deformation (permanent deformation) through processes like rolling, bending, or stretching. This deformation results in an increase in the material's strength and hardness. The same principles of work hardening apply to AM metals, although the specific behaviours can be influenced by factors unique to the AM process.

In the following, the literature related to temperature effects on work hardening, microstructure and anisotropy,

✉ Ahmad Serjouei
ahmad.serjouei@ntu.ac.uk

¹ Department of Engineering, School of Science and Technology, Nottingham Trent University, Nottingham NG11 8NS, UK

work hardening models and theoretical approaches, tensile behaviour, and toughness is reviewed, and then the research gaps and objectives of our research are presented.

Song et al. [7] performed tensile testing on AlSi10Mg at 35 °C and 200 °C build platform temperatures. The results at 200 °C showed exaggerated anisotropy in the strain hardening capacity in the vertical direction in comparison to the 35 °C sample due to the fine microstructure of the 35 °C sample compared to the 200 °C sample. Van Cauwenbergh et al. [8] examined the multi-scale structure–property relationship of PBF-LB-processed and heat-treated AlSi10Mg. They found that the rapid solidification inherent to PBF-LB leads to a fine cellular microstructure, which significantly influences the alloy's hardening capacity.

Bao et al. [9] showed that the stress-relieved PBF-LB AlSi10Mg has a more homogeneous microstructure, which correlated directly to the enlargement in elongation. They concluded that the tensile fracture of the stress-relieved samples is less likely to propagate along the microstructure boundaries because the applied load is perpendicular to the building orientation. Takata et al. [10] examined the microstructure of Al-Si-based alloys produced by PBF-LB and determined that nano-sized particles might restrict dislocation movement, thereby improving work hardening. This aligns with the reduced work hardening rate after annealing. Zhao et al. [11] focused on the microstructure effect on the mechanical performance of AlSi10Mg and found that the shape of the Si-rich network had a significant impact on the strain hardening. They discussed that anisotropic strength is due to the elongated Si-rich network, while anisotropic toughness is due to the way the melt pools are arranged. Li et al. [12] studied the tensile behaviour of PBF-LB AlSi10Mg alloy printed in 0°, 15°, 30°, 45°, 60°, 75°, and 90° orientations and found that the 60° sample presents a good combination of ductility and high strength, owing to its work hardening ability.

Zhang et al. [13] used the Kocks-Mecking model [14] and the Voce model to predict the strain hardening behaviour of annealed PBF-LB AlSi3.5Mg2.5. Ming et al. [15] used Hollomon's equation to compare work hardening in AlSi7Mg with heat-treated AlSi7Mg and found work hardening exponents of 0.23, 0.20, 0.20, and 0.17 for as built, direct aging, annealing, and solution and aging, respectively. Similarly, Konda Gokuldoss [16] used Hollomon's equation to analyse the work hardening of PBF-LB Al-12Si alloy and found a work hardening exponent of 0.26. The premature failure during tensile testing negates uniform elongation associated with the structural defects. Chen et al. [6] used Hollomon's equation to analyse the work hardening behaviour of PBF-LB AlSi10Mg, and a large work hardening exponent of 0.252 was observed. Baxter et al. [17] used an extended Hollomon's equation to fit the direct metal laser sintered AlSi10Mg printed in a horizontal direction and used the

Chang-Asaro hardening equation to fit the vertically printed results, both with hyperbolic tangent and exponential decay functions involved. Both theoretical models compared well with experiments at all strain rates. Clyne and Campbell [18] underlined the basis of tensile testing, producing an in-depth theoretical analysis of the process of necking. The plot of true stress against true strain provides both plasticity and failure characteristics for the specific material of interest. Failure is usually preceded by some degree of necking, a phenomenon closely associated with work hardening. Instability is anticipated when an increase in local strain does not result in a corresponding increase in load. Song et al. [1] used the stress ratio comparison in each Al and Si phase of PBF-LB AlSi10Mg to present the strength in the strain hardening stage and further summarised that the strain gradient effect is anticipated to considerably postpone the onset of damage and diminish the damage density.

Due to variations in printing direction, the accumulation of thermal stresses in the workpiece can result in differences in mechanical properties [19]. Fiocchi et al. [5] presented the tensile test results of PBF-LB AlSi10Mg for horizontal and vertical printing orientations in as-built and heat-treated conditions. Annealing at 244 °C effectively stress relieved the material while maintaining its strength due to the presence of the continuous Si network. Takata et al. [20] performed tensile testing in the X, Y, and Z directions of PBF-LB AlSi10Mg and concluded that the fine Si particles enhance the local work hardening in the α -Al matrix, leading to crack initiation at the interfaces between the melt pools. Dong et al. [21] discussed the trade-off between strength and ductility and how improving the work hardening rate delays necking, leading to increased ductility. They discussed how toughness (area under the stress–strain curve) is an indicator of both strength and ductility and showed that there is an optimum work hardening rate that will produce the ideal overall mechanical property. Wan et al. [22] studied the ultimate tensile stress (UTS) and toughness of as-built PBF-LB AlSi10Mg post-processed with three different heat-treated conditions. They found that the overall toughness is increased through the varying heat treatment, which corresponds to the major increase in the elongation at fracture. This increase was attributed to the decrease in the number of microvoids in the as-built samples after applying heat treatments. Tang et al. [23] demonstrated that applying direct aging heat treatment (160 °C for 4 h) can alleviate approximately 40% of the residual stress in the AlSi10Mg alloy, leading to an improvement in fracture toughness.

While most of the research efforts have utilised traditional methods (original Voce and Hollomon equations) to approximate work hardening, very few studies have proposed improvements to these models or directly compared them to identify which is superior. Furthermore, no attempts have been made to link work hardening parameters to other

mechanical properties, such as hardness, of AM materials. Therefore, the objective of this study is to compare Hollomon vs. Voce models for PBF-LB AlSi10Mg (including improved fitting via Levenberg–Marquardt (LM) least square method) and to propose a unique method to estimate Vickers hardness of AM materials purely from tensile testing and the use of work hardening from tensile data.

2 Background

2.1 Work hardening approximation models

The work hardening approximation methods are briefly reviewed in this section.

2.1.1 Hollomon equation

The general form of the Hollomon equation is given by [24]:

$$\sigma = K_H \epsilon^{n_H} \tag{1}$$

where σ is the mechanical true stress, ϵ is the mechanical true strain, K_H is the Hollomon strength coefficient, and n_H is the Hollomon work hardening exponent.

2.1.2 Voce equation

The general form of the Voce equation is given by [25]:

$$\sigma = \sigma_s - K_V \times \exp(n_V \epsilon) \tag{2}$$

where σ_s is the saturation stress, $\frac{d\sigma}{d\epsilon}$ is the work hardening rate, and n_V and K_V are Voce equation constants. The differential followed by the logarithmic manipulation of Eq. 2 will give:

$$\ln \left| \frac{d\sigma}{d\epsilon} \right| = \ln(n_V K_V) + n_V \epsilon \tag{3}$$

It should be noted that the logarithm of absolute values is considered to ensure the argument remains positive, thereby avoiding the logarithm of negative values. A plot of $\ln \left| \frac{d\sigma}{d\epsilon} \right|$ against ϵ produces a straight line of constant n_V as the slope and $\ln(n_V K_V)$ as the y-intercept. From this graphical interpretation, constant n_V and subsequently constant K_V can be obtained purely from true stress and true strain as inputs [25]. It should be noted that sometimes K_V is written as $(\sigma_s - \sigma_Y)$. At large strains, all curves converge towards a finite saturation stress. Therefore, there is a finite value that can be achieved and utilised in the Voce equation [26]. In most cases this saturation stress is presented at the asymptotic value of the top of the flow curve [26]. Southern et al. [27] used an extended version of the Voce approximation to approximate work hardening given by:

$$\sigma = \sigma_s - (\sigma_s - \sigma_Y) \times \exp\left(-\frac{\epsilon}{\epsilon_0}\right) \tag{4}$$

A comparison of Eqs. 2 and 4 shows that the constant K_V is the subtraction of the yield stress (YS), σ_Y , from the saturation stress, σ_s , with both constant K_V and the YS being previously obtained. A simple rearrangement of Eq. 4 gives the saturation stress as:

$$\sigma_s = K_V + \sigma_Y \tag{5}$$

From both the plot of $\ln d\sigma/d\epsilon$ against ϵ along with Eq. 5, all inputs can therefore be obtained to formulate the Voce approximation [25].

2.2 UTS-hardness and YS-hardness relationships

Because we aim to estimate hardness from tensile behaviour, we summarise here empirical strength-hardness correlations from literature (Eqs. 6 and 7). For fine-grained and ultra-fine-grained materials processed using constrained groove pressing method, empirical relationships between UTS (σ_u) and YS (σ_Y) and Vickers hardness, H_V , are given by Eqs. 6 and 7 [28]:

$$H_V = \left(\frac{\sigma_Y}{3}\right) \times (0.1)^{-n_H} \tag{6}$$

$$H_V = \left(\frac{\sigma_u}{2.9}\right) \times (1 - n_H) \times \left[\frac{12.5 \times n_H}{1 - n_H}\right]^{n_H} \tag{7}$$

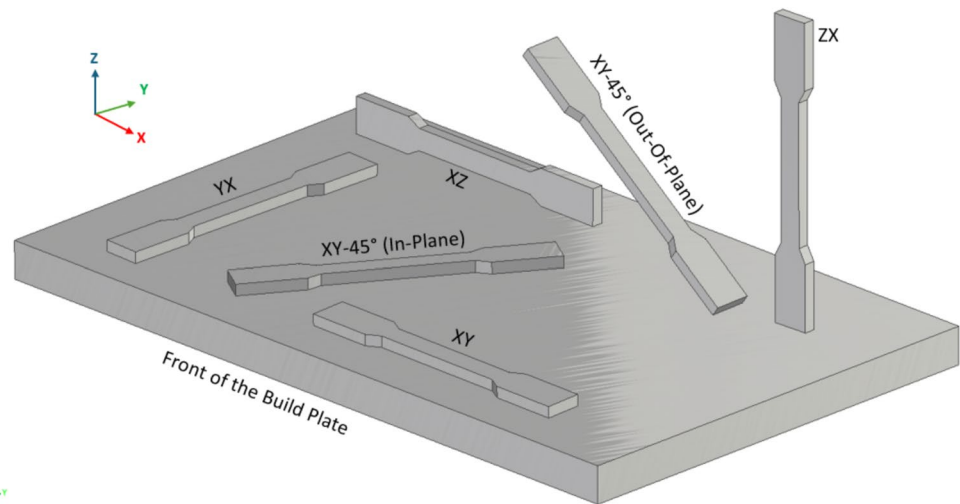
where n_H is the Hollomon work hardening exponent.

3 Material and methods

The EOS M280 3D printer was used to fabricate the AlSi10Mg tensile specimens. Details of printing parameters, tensile sample dimensions, tensile test and hardness measurements can be found in Ref. [29]. Vickers hardness measurements (at a 5-kgf load) were conducted on the cross-sections perpendicular to the specimen’s longitudinal axis using a Duramin-500 universal hardness tester. Hardness was evaluated in both the gauge length and the gripping section of the specimens. Testing followed the ISO 6507–1 standard [30], with five indentations performed on each specimen to ensure accuracy.

Figure 1 shows the six orientations of the tensile specimens. The XY, XY-45° (in-plane) and YX are parallel to the build plate at angles of 0°, 45° and 90°, respectively. The XY-45° (out of plane) and ZX are out of plane at angles of 45° and 90°, respectively, while XZ is printed perpendicular to the build plate. Five specimens of each orientation were printed to ensure repeatability of results. All specimens

Fig. 1 The printing orientations of PBF-LB AlSi10Mg



underwent stress relief annealing for 2 h at 300 °C. Tensile tests were performed, at room temperature, on an MTS 810 machine (250-kN load capacity, 80-mm stroke) at a strain rate of $1 \times 10^{-3} \text{ s}^{-1}$ under displacement control. Furthermore, the hardening capacity and toughness were calculated using tensile test data as follows: Hardening capacity, H_c , was calculated in relation to the UTS, σ_u , and YS, σ_Y , using $H_c = \frac{\sigma_u - \sigma_Y}{\sigma_Y}$ [31], and toughness was calculated by taking numerical integration of the true stress–strain curve up to fracture.

Voce and Hollomon approximation equations are used to model the work hardening of AlSi10Mg for all printing orientations. To enable a comprehensive comparison of Hollomon and Voce parameters for heat-treated and as-built AlSi10Mg samples, stress–strain curve data tensile were derived from the literature or, if not explicitly available, digitised from their stress–strain graphs, and then Hollomon and Voce equations were fit to them. Both Voce and Hollomon parameter sets approximate the true stress–true strain relationship until the onset of necking. Therefore, the plots of Voce and Hollomon approximations are only presented from the yield strength to the onset of necking. The LM method, explained in the Appendix, was used to find optimum parameters for both the Voce and Hollomon methods to improve their fit to the experimental data. A local sensitivity analysis using a one-at-a-time (OAT) approach [32] is performed to determine each corresponding equation (Hollomon or Voce) sensitivity to the individual parameters in the equation. The method varies each parameter by a 5% variance to ensure isolation of its effect on the model's response. The method utilises the R^2 value as the measurement metric to present the effect of varying the individual parameter; the larger the change in the baseline R^2 value, the greater the effect of varying that specific parameter has caused, and the more sensitive the overall equation is to said parameter.

4 Results and discussion

4.1 Tensile properties

Figure 2a [29] shows the engineering stress, σ_n , vs. engineering strain, ϵ_n , curves for AlSi10Mg alloy printed in different orientations. They can be converted into true stress, σ_T , vs. true strain, ϵ_T , plots using the conservation of volume during plastic deformation, namely $\sigma_T = \sigma_n(1 + \epsilon_n)$ and $\epsilon_T = \ln(1 + \epsilon_n)$. The true stress–true strain graphs are presented in Fig. 2b. Work hardening rate (which is the rate of change of true stress with true strain, i.e., $\frac{d\sigma_T}{d\epsilon_T}$) vs. true strain for different build orientations is shown in Fig. 2c.

Table 1 lists the tensile properties and hardening capacity for PBF-LB AlSi10Mg with different heat-treatment and build-orientation conditions. The YS, σ_Y , was determined by the point of interception of the true stress–true strain graph with the 0.2% offset line.

4.1.1 Considère's criterion and onset of necking

The uniform elongation of the material is related to the occurrence of plastic instability or necking which is related to the Considère's criterion, $\sigma_T \geq \frac{d\sigma_T}{d\epsilon_T}$ [37]. Once a neck starts to form in a material, there is a large increase in true stress (flow stress) at the location of the neck, leading to more strain which then leads to more necking. This cycle then accelerates necking which leads to the fracture of the sample [18]. Work hardening counters this cyclic effect however, since the higher strain experienced at the neck will require a higher stress at that point to further increase strain due to the nature of the stress–strain curve. Generally, work hardening is sufficient to have uniform straining and prevent early necking. However, work hardening rate decreases with

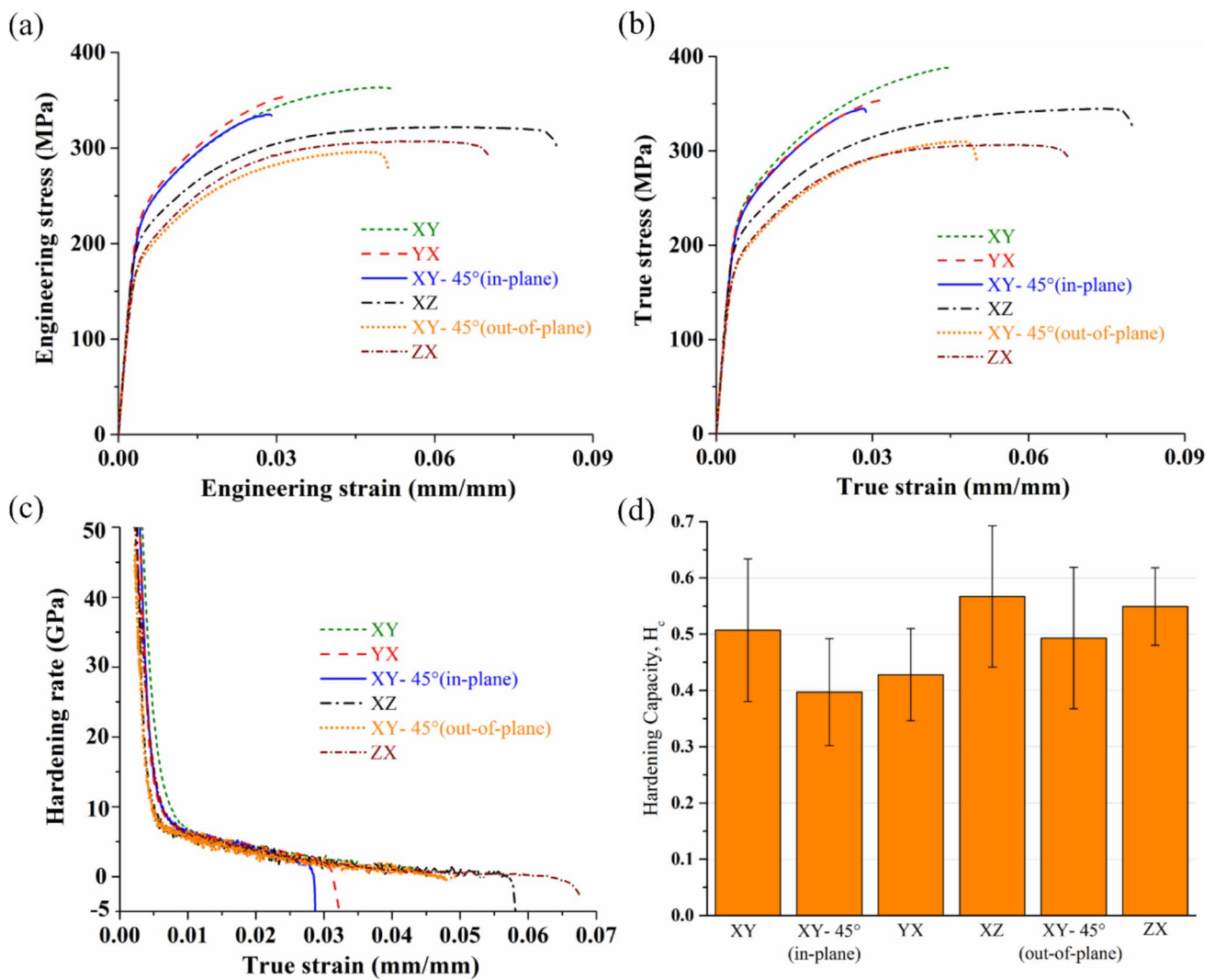


Fig. 2 Room temperature tensile properties for different building orientations: **a** engineering stress vs. engineering strain, **b** true stress vs. true strain, **c** work hardening rate vs. true strain, and **d** hardening capacity

increasing strain, meaning there will be a point at which work hardening will not be sufficient to delay the cycle discussed [18]. This point is defined by Armad Considère and is commonly known as Considère's criterion. Considère stated the necking is anticipated to initiate when the local strain rises to a point where there is no corresponding increase in the overall load. This exact point is found when work hardening rate curve and the true stress curves meet for a given sample, and hence, necking is only expected to occur after each said curves have crossed each other's paths. To understand whether each sample achieves uniform elongation, a plot of both work hardening rate and true stress against true strain was obtained [16]. It should be noted that detecting the onset of necking is a challenging task. Multi-camera DIC systems have the potential to accurately detect the onset of localised necking in uniaxial testing [38].

Due to the large distortion in the work hardening rate curve caused by a large set of data recorded by the MTS-810 machine, exponential smoothing with a damping ratio of 0.9 is used to reduce noise within the data. This smoothed work hardening rate curve was then used to determine the point where the work hardening rate and true stress curves meet, as shown in Fig. 3.

The two curves for XY and YX samples do not cross which shows that there is no necking occurring for these two samples, and this is also evident from Fig. 2b as there is no softening after UTS and a premature fracture occurs. For XY_45° (in-plane), the two curves meet slightly earlier than the break strain, and this can be related to the slight softening and possible necking after UTS in Fig. 2b. For samples XZ, XY_45° (out-of-plane), and ZX, the work hardening rate and true stress curves meet comparatively earlier than

Table 1 YS (σ_Y), UTS (σ_u), and elongation at fracture (ϵ_f) and hardening capacity (H_c) for PBF-LB AlSi10Mg under different heat treatments and build orientations (note: current work values are mean \pm SD for 5 samples. Literature values are as reported (single measurements or averages where available))

Building orientation	Heat treatment	σ_Y (MPa)	σ_u (MPa)	ϵ_f (%)	H_c^*	Ref
XY	300 °C/2 h	243.60 \pm 7.20	366.60 \pm 4.60	4.70 \pm 0.30	0.50 \pm 0.12	Current work
XY_45° (in-plane)	300 °C/2 h	238.30 \pm 7	332.60 \pm 4.90	2.80	0.39 \pm 0.09	Current work
YX	300 °C/2 h	244.50 \pm 2.10	349 \pm 7	3 \pm 0.20	0.43 \pm 0.08	Current work
XZ	300 °C/2 h	209.3 \pm 2.90	327.8 \pm 8.60	7.20 \pm 1.10	0.57 \pm 0.12	Current work
XY_45° (out-of-plane)	300 °C/2 h	198.30 \pm 3.60	295.80 \pm 7.10	4.60 \pm 0.50	0.49 \pm 0.12	Current work
ZX	300 °C/2 h	197.70 \pm 3.50	306.10 \pm 1.40	5.90 \pm 1.50	0.55 \pm 0.07	Current work
ZX	35 °C build platform temperature	270	440	2.40	0.63	[1]
ZX	200 °C build platform temperature	112	340	1.80	2.04	[1]
XY	35 °C build platform temperature	230	430	9.40	0.87	[1]
XY	200 °C build platform temperature	100	290	9.20	1.90	[1]
XZ	170 °C/90 min	312	446	3.50	0.43	[5]
XZ	244 °C/180 min	227	375	4.70	0.65	[5]
XZ	290 °C/45 min	230	373	5.60	0.62	[5]
ZX	170 °C/90 min	287	450	2.60	0.57	[5]
ZX	244 °C/180 min	215	378	4.70	0.76	[5]
ZX	290 °C/45 min	218	376	9.50	0.72	[5]
XY	-	200	300	18	0.50	[9]
XY	-	250	510	8	1.04	[10]
XY	300 °C/2 h	220	290	16	0.32	[10]
XY	530 °C/2 h	150	280	15	0.87	[10]
XY	-	279	475	7	0.70	[20]
XY	300 °C/2 h	180	285	18.60	0.58	[20]
XY	530 °C/6 h	153	269	18.30	0.76	[20]
ZX	-	230	480	5	1.09	[20]
ZX	300 °C/2 h	175	290	14.20	0.66	[20]
ZX	530 °C/6 h	139	245	18.20	0.76	[20]
ZX	-	184 \pm 5	292 \pm 3	18.10 \pm 1	0.59	[33]
ZX	-	183 \pm 5	301 \pm 3	17.10 \pm 1	0.64	[33]
ZX	-	190 \pm 5	316 \pm 3	16.90 \pm 1	0.66	[33]
ZX	-	185 \pm 5	330 \pm 3	15.50 \pm 1	0.78	[33]
ZX	-	195 \pm 5	338 \pm 3	14.50 \pm 1	0.73	[33]
XY	-	185 \pm 6	285 \pm 2	22.80 \pm 0.70	0.54	[33]
XY	-	184 \pm 6	299 \pm 2	21 \pm 0.70	0.63	[33]
XY	-	184 \pm 6	312 \pm 2	22.40 \pm 0.70	0.70	[33]
XY	-	185 \pm 6	323 \pm 2	19.60 \pm 0.70	0.75	[33]
XY	-	187 \pm 6	331 \pm 2	18.20 \pm 0.70	0.77	[33]
XY	-	232	415	8	0.79	[34]
ZX	-	204	437	5.50	1.14	[34]
XY	-	245	380	8.50	0.55	[35]
ZX	-	240	350	8.20	0.46	[35]
XY	-	224 \pm 27	486	6.90 \pm 0.80	1.17	[36]
XY	530 °C/2 h	252	512	4.90 \pm 0.60	1.03	[36]
XY	530 °C/604 h plus SHT**	195	447	4.50 \pm 0.30	1.29	[36]
XY	SHT**	126	268	17 \pm 1.70	1.13	[36]
XY	530 °C/5 h plus SHT**	251	341	7.10 \pm 1.30	0.36	[36]
XY	530 °C/604 h	109	180	19.90 \pm 1.40	0.65	[36]

*Hardening capacity, H_c , was calculated in relation to the UTS, σ_u , and YS, σ_Y , using $H_c = \frac{\sigma_u - \sigma_Y}{\sigma_Y}$ [31]

**Solution heat-treated (SHT) for 5 h at 530 °C, quenched in room temperature water, and then aged at 170 °C [36]

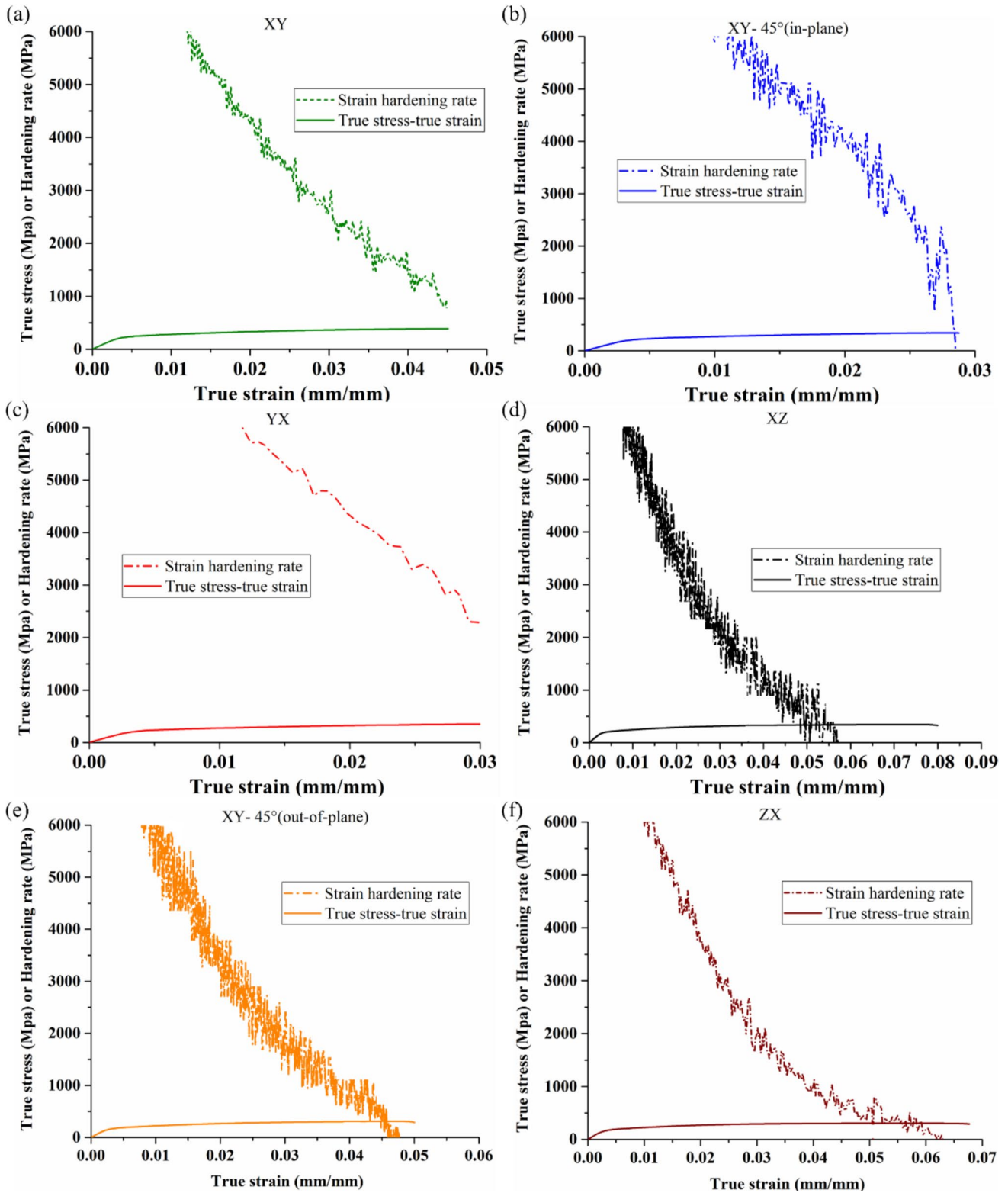


Fig. 3 Work hardening rate and true stress vs. true strain curves for **a** XY, **b** XY_{45°} (in-plane), **c** YX, **d** XZ, **e** XY_{45°} (out-of-plane), and **f** ZX build orientations

XY_{45°} (in-plane) sample which shows possible necking occurs earlier, and this can be related to the more obvious softening occurring after UTS for these three samples in Fig. 2b. It should be noted that Considère's criterion can only approximate the onset of necking and cannot provide exact strain at which necking occurs. High speed imaging of the sample while undergoing tensile testing might be used to find out the onset of necking.

4.2 Work hardening approximations

4.2.1 Original Voce and Hollomon approximations

Figure 4 shows original Voce and Hollomon approximations compared with the experimental true stress–true strain curves for different build orientations, and the coefficient of determination (COD), R^2 , up to three decimal places, is also presented to show the goodness of fit. The small difference shown in the R^2 value for the XY, XY_{45°} (in-plane), and the YX orientation shows slight magnitudes of difference between the Voce and Hollomon approximations, with all showing the Hollomon approximation being slightly more accurate. For the XZ, XY_{45°} (out-of-plane), and ZX orientations, the Voce approximation showed superior accuracy over the Hollomon approximation, with much larger differences in the magnitude of the R^2 values.

Zhao et al. [29] showed that the Hollomon equation tended to overestimate stress at greater deformations, whereas the Voce equation provided a more accurate fit across the entire flow curve. This is shown throughout the majority of orientations in Fig. 4 and is especially prominent in the ZX orientation, with the experimental Hollomon curve value ending at 343.3 MPa in comparison to the actual experimental value of 325.5 MPa, giving the endpoint of the Hollomon approximation off by 17.6 MPa. The YX orientation Hollomon curve differs from this pattern; however, it shows an almost exact approximation of the experimental true stress–strain curve, producing a value of 377.1 MPa, while the experimental endpoint is 376.1 MPa, showing only a difference of 1 MPa. This phenomenon, known as saturation, is the work hardening curve's ability to plateau with increasing strain. The YX orientation stress–strain curve presents this saturation noticeably less than all other orientations, with little of a plateau and more of a comparatively steep gradient to finish the curve. The Voce equation gives a more accurate approximation when the curve shows a clear saturation [36]. Since the YX graph presents little saturation, the Voce equation for this direction does not show better accuracy over the Hollomon equation. The Voce equation provides a more accurate representation of the flow curve compared to the Hollomon equation, as shown by the overall improved R^2 value, along with the Hollomon approximations, producing overestimations of the flow curves.

The original Hollomon and Voce parameters extracted from the analysis of the digitised stress–strain data gathered from the literature for PBF-LB AlSi10Mg with different heat-treatment and build-orientation conditions are provided in Table 2.

Table 3 lists the range of original Voce and Hollomon parameters as well as hardening capacity ranges for as-built (AB) and heat-treated (HT) conditions. Comparing AB and HT AlSi10Mg, both $n_{\text{Horiginal}}$ and $K_{\text{Horiginal}}$ exhibits consistent ranges, with the AB range encompassing the HT range for n_{H} and a major overlap for the HT and AB range for $K_{\text{Horiginal}}$. Recent studies have also presented $n_{\text{Horiginal}}$ to be in the range of 0.18–0.25, aligning inside with the range presented for the AB AlSi10Mg in [39]. The Voce saturation stress parameters, $\sigma_{\text{Soriginal}}$, for HT samples show larger upper and lower limits with large overlap compared to AB samples. Similar conclusions are drawn with $K_{\text{Voriginal}}$, but for $n_{\text{Voriginal}}$, the HT samples show a larger upper limit only, still with a large overlap in ranges. The high variability in some ranges for HT samples can be due to the diverse heat-treatments applied across the literature. These variations produce significantly different stress–strain curves, consequently affecting Voce and Hollomon parameters.

In summary, this section compared Voce and Hollomon approximations against experimental true stress–strain curves for different build orientations, showing that Hollomon provides a slightly better fit for in-plane orientations, while Voce is more accurate for out-of-plane orientations due to its ability to capture saturation effects. Additionally, Voce parameters exhibit higher variability in heat-treated samples, likely due to diverse heat-treatment processes, influencing the material's hardening behaviour.

4.2.2 Improved Voce and Hollomon approximations using LM method

Figure 5 shows the Voce and Hollomon approximations obtained from the LM method (see Appendix) compared with the true stress–true strain curves for different build orientations. Comparing the parameters predicted from the previous analysis to the LM method shows an increase in the corresponding R^2 values for both the Voce and Hollomon approximations, clearly presenting the margin of error for the previous methods for both the Voce and Hollomon. The R^2 values for the Voce approximation using the LM method (Voce_LM) show close to perfect R^2 values of 0.999, a large increase from the previously predicted approximations. The Hollomon approximations using the LM method (Hollomon_LM) also show an increase in R^2 values, but only marginally, with the maximum difference in R^2 value from the original prediction to the LM method prediction being 0.002 (for the XZ direction). With such improved R^2 values for the Voce_LM method, it clearly shows the superiority in

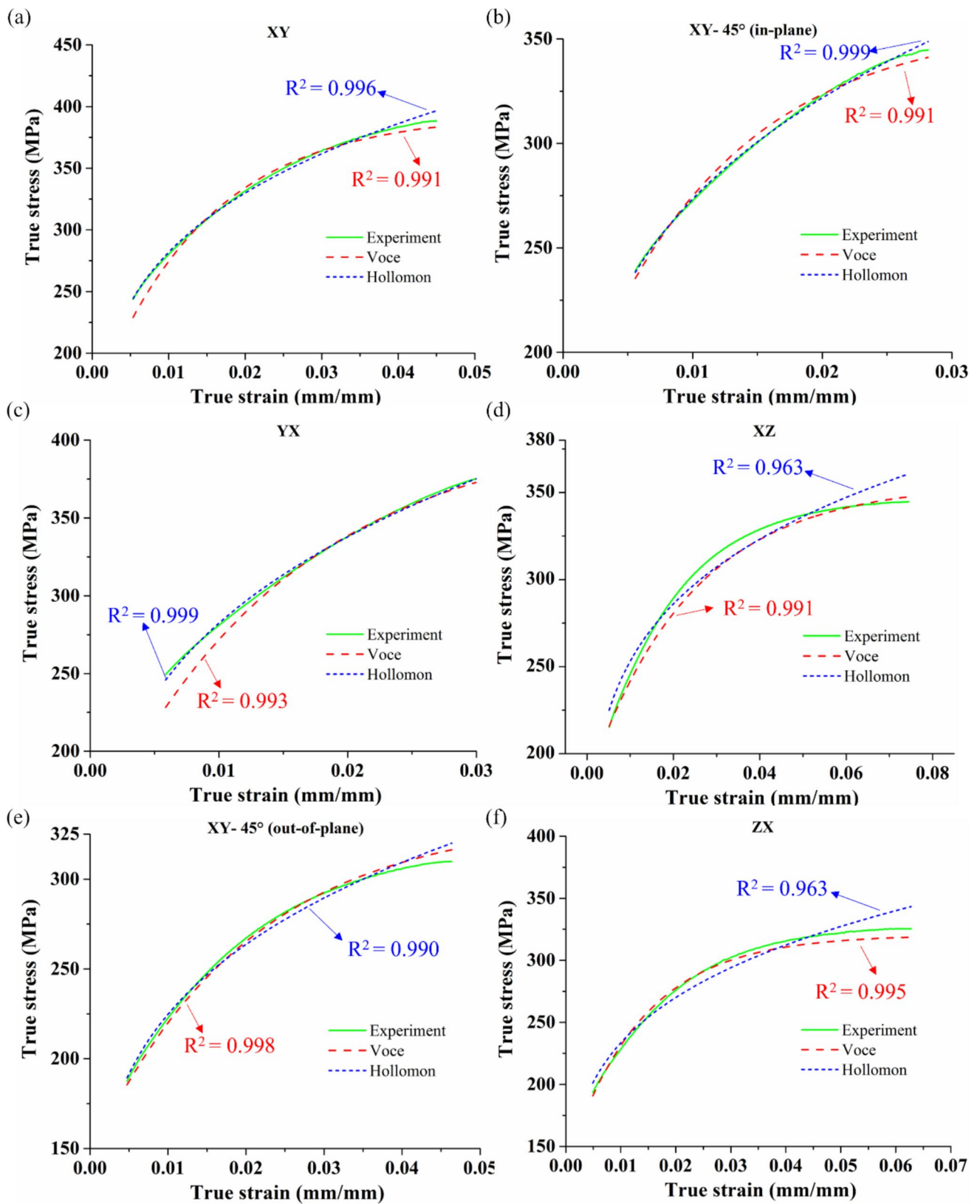


Fig. 4 Original Voce and Hollomon approximations compared with the true stress-true strain curves for **a** XY, **b** XY_{45°} (in-plane), **c** YX, **d** XZ, **e** XY_{45°} (out-of-plane), and **f** ZX build orientations. Coefficient of determination (COD), R^2 , is also presented to show the goodness of fit

Table 2 The original Hollomon parameters (work hardening exponent, $n_{Horiginal}$, and strength constant, $K_{Horiginal}$) and Voce parameters (saturation stress, $\sigma_{Soriginal}$, work hardening exponent, $n_{Voriginal}$ and strength constant, $K_{Voriginal}$) used for work hardening approximation for PBF-LB AlSi10Mg with different heat-treatment and build-orientation conditions (note: $n_{Horiginal}$, $n_{Voriginal}$, and $K_{Voriginal}$ are dimensionless)

Orientation	Heat treatment	$n_{Horiginal}$	$K_{Horiginal}$ (MPa)	$\sigma_{Soriginal}$ (MPa)	$n_{Voriginal}$	$K_{Voriginal}$	Ref
XY	300 °C/2 h	0.22	778.50	394.06	63.95	220	Current work
XY_45° (in-plane)	300 °C/2 h	0.23	792.30	358.12	87.78	200.23	Current work
YX	300 °C/2 h	0.24	831.50	409.38	66.39	267.28	Current work
XZ	300 °C/2 h	0.19	615.50	371.66	42.13	172.88	Current work
XY_45° (out-of-plane)	300 °C/2 h	0.23	660.40	321.56	50.11	189.70	Current work
ZX	300 °C/2 h	0.22	647.80	320.48	73.74	186.36	Current work
ZX	35 °C build platform temperature	0.24	1310	823.51	25.63	444.46	[1]
ZX	200 °C build platform temperature	0.19	820.40	523.33	36.27	249.47	[1]
XY	35 °C build platform temperature	0.24	1256	799.01	24.53	428.41	[1]
XY	200 °C build platform temperature	0.17	696.50	496.93	29.06	225.44	[1]
XZ	170 °C/90 min	0.20	857.40	527.98	44.03	247.81	[5]
XZ	244 °C/180 min	0.22	731.80	406.03	58.44	198.03	[5]
XZ	290 °C/45 min	0.20	624	360.78	56.93	165.31	[5]
ZX	170 °C/90 min	0.26	1039.90	498.40	63.15	283.10	[5]
ZX	244 °C/180 min	0.29	949.70	413.60	65.82	250.13	[5]
ZX	290 °C/45 min	0.27	832.20	443.13	67.24	288.49	[5]
XY	-	0.25	959.50	572.22	29.77	315.02	[10]
XY	300 °C/2 h	0.15	441.90	371.34	38.88	179.02	[10]
XY	530 °C/2 h	0.19	431.70	305.12	21.05	153.85	[10]
XY	-	0.42	358.70	286.83	18.58	9.19	[20]
XY	300 °C/2 h	0.19	532.30	330.18	56.37	330.18	[20]
XY	530 °C/6 h	0.21	450.60	301.06	21.92	162.25	[20]
ZX	-	0.36	1434.30	648.92	27.93	415.55	[20]
ZX	300 °C/2 h	0.19	532.30	346.20	52.94	153.30	[20]
ZX	530 °C/6 h	0.21	428.70	301.45	8.038	162.99	[20]
ZX	-	0.17	482 ± 12	402.37	28.68	217.28	[33]
ZX	-	0.19	542 ± 12	295.02	48.84	117.22	[33]
ZX	-	0.20	586 ± 12	299.58	65.51	150.84	[33]
ZX	-	0.21	610 ± 12	315.37	50.86	149.27	[33]
ZX	-	0.26	673 ± 12	330.45	49.83	163.08	[33]
XY	-	0.16	453 ± 10	338.15	52.48	170.10	[33]
XY	-	0.18	511 ± 10	284.38	44.81	97.91	[33]
XY	-	0.19	550 ± 10	297.62	47.71	117.17	[33]
XY	-	0.20	590 ± 10	310.96	46.09	135.83	[33]
XY	-	0.22	633 ± 10	323.99	49.86	149.47	[33]
XY	-	0.23	903.20	573.21	26.28	301.87	[34]
ZX	-	0.27	1001.80	561.13	33.44	333.77	[34]
XY	-	0.145	281.46	447.77	39.04	217.85	[35]
ZX	-	0.206	281.12	421.20	32.55	196.26	[35]
XY	-	-	-	573 ± 4	33.70 ± 1.30	329	[36]
XY	530 °C/2 h	-	-	583 ± 7	50.1 ± 2.60	332	[36]
XY	530 °C/604 h plus SHT*	-	-	511 ± 6	52.2 ± 1.90	280	[36]
XY	SHT*	-	-	297 ± 7	29.2 ± 2.20	149	[36]
XY	530 °C/5 h plus SHT*	-	-	356 ± 7	96.90 ± 12.40	85	[36]
XY	530 °C/604 h	-	-	194 ± 4	54.70 ± 2.40	77	[36]

*Solution heat treated (SHT) for 5 h at 530 °C, quenched in room temperature water, and then immediately transitioned for aging at 170 °C extracted [36]

Table 3 Range of original Hollomon parameters (work hardening exponent, $n_{Horiginal}$; and strength constant, $K_{Horiginal}$) and Voce parameters (saturation stress, $\sigma_{Soriginal}$; work hardening exponent, $n_{Voriginal}$;

and strength constant, $K_{Voriginal}$), as well as hardening capacity ranges for as-built (AB) and heat-treated (HT) conditions

Condition	$n_{Horiginal}$	$K_{Horiginal}$ (MPa)	$\sigma_{Soriginal}$ (MPa)	$n_{Voriginal}$	$K_{Voriginal}$	H_c
AB	0.145–0.42	281.10–1434.30	284.38–648.92	18.58–65.51	9.19–415.55	0.46–1.31
HT	0.15–0.29	428.70–1310	301.06–823.51	8.04–109.30	77–444.46	0.36–1.29

approximating the work hardening curve compared to the Hollomon_LM approximation. Similar overestimations of the flow curve from the previous method for the Hollomon approximations are shown in Fig. 5, further signifying the superiority of the Voce equation. The superiority is also shown with the LM method, in comparison to the original methods discussed in Sect. 4.2.1, used to achieve both the Voce and Hollomon equations, supported by the increase in the R^2 value. The Hollomon_LM and Voce_LM parameters for PBF-LB AlSi10Mg with different build-orientation conditions are provided in Table 4.

To determine which parameters have the greatest impact on the accuracy of the improved Voce and Hollomon model predictions, a sensitivity analysis was performed, which will be discussed in the next section.

4.2.2.1 Sensitivity analysis For the sensitivity analysis, one parameter was varied by $\pm 5\%$, from the original values presented in Table 4, while keeping other(s) constant and observing the changes in the R^2 values from the ones obtained from the Hollomon_LM and Voce_LM as baseline values (baseline values are presented in Fig. 5). The sensitivity analysis results, for the Hollomon_LM and Voce_LM methods, including parameter percentage change, associated R^2 value, and deviation from the original R^2 value for different printing orientations, are presented in Tables 5 and 6, respectively. Figure 6 shows the representative sensitivity analyses of the Hollomon_LM and Voce_LM methods for the sample of XY_45° (out-of-plane) orientation.

For the Hollomon_LM method, sensitivity analyses showed that for all the sample orientations, except the YX orientation, varying K_{HLM} resulted in a larger deviation from the baseline R^2 value over the n_{HLM} parameter. The largest deviation recorded was observed for the decrease in K_{HLM} by 5% ($K_{HLM} - 5\%$), for the XY_45° (in-plane) orientation producing a variance of 0.2234 and a corresponding R^2 value of 0.7746. The largest deviation for varying the n_{HLM} parameter was found with the YX orientation producing a variance of 0.2152 and a corresponding R^2 value reduced to 0.7828. The overall trend for the sensitivity analysis is that the Holloman equation is the most sensitive to K_{HLM} and less sensitive to n_{HLM} .

For the Voce_LM method, the results showed that for all the printing orientations, the most sensitive parameter out of $\sigma_{S_{LM}}$, $n_{V_{LM}}$, and $K_{V_{LM}}$ is $\sigma_{S_{LM}}$. This can be seen in Fig. 6:

as $\sigma_{S_{LM}}$ increased or decreased by 5%, the model predictions move up or down along the Y -axis (stress axis) while for the other two parameters, the change in model predictions is comparatively less significant. The largest deviation from the baseline R^2 value through varying $\sigma_{S_{LM}}$ was 0.3728 reducing the R^2 value to 0.6252. The largest deviation from the baseline R^2 value through varying $K_{V_{LM}}$ was 0.0494 reducing the R^2 value to 0.9496. The largest deviation from the baseline R^2 value through varying $n_{V_{LM}}$ was 0.0468 reducing the R^2 value to 0.9522. For the Hollomon_LM method, sensitivity analyses showed that for all the sample orientations, $\sigma_{S_{LM}}$ is the most sensitive parameter showing higher deviations from baseline compared to the other two parameters. For all the sample orientations, except the XZ orientation, $K_{V_{LM}} \pm 5\%$ showed higher deviations compared to $n_{V_{LM}} \pm 5\%$, meaning that $K_{V_{LM}}$ was the second most sensitive followed by $n_{V_{LM}}$. For the XZ orientation, $n_{V_{LM}} + 5\%$ deviation is larger than that of the $K_{V_{LM}} - 5\%$ deviation; however $K_{V_{LM}}$ still holds the largest deviation (comparing only $K_{V_{LM}}$ or $n_{V_{LM}}$) with the “ $K_{V_{LM}} + 5\%$ ” result producing a deviation of 0.0494 which is greater than the largest deviation of all other $K_{V_{LM}}$ and $n_{V_{LM}}$ results for the XZ orientation.

4.3 Hardening capacity

Since hardening capacity ($H_c = \frac{\sigma_u - \sigma_y}{\sigma_y}$) is reliant on the UTS, σ_u , and YS, σ_y , it directly represents to the height of the work hardening section of the stress–strain curve. Hardening capacity for different build orientations are shown in Fig. 2d. Regarding current work only, the hardening capacities have large overlapping variance between each orientation with on average the XZ orientation having the largest hardening capacity and XY_45° (in-plane) having the lowest hardening capacity.

The current H_c values along with additional literature hardening capacity values are presented in Table 1 and the corresponding range of the discovered H_c values are split into heat-treated (HT) and as-built (AB) ranges shown in Table 3. Both ranges present a large overlap with HT and AB samples, with the AB range showing a marginally larger upper and lower limit (0.46–1.31) than that of the HT range (0.36–1.29). The large similarity in the H_c ranges could be caused by the large variance of printing parameters for both AB and HT samples. Wang et al. [40] presents a similarity

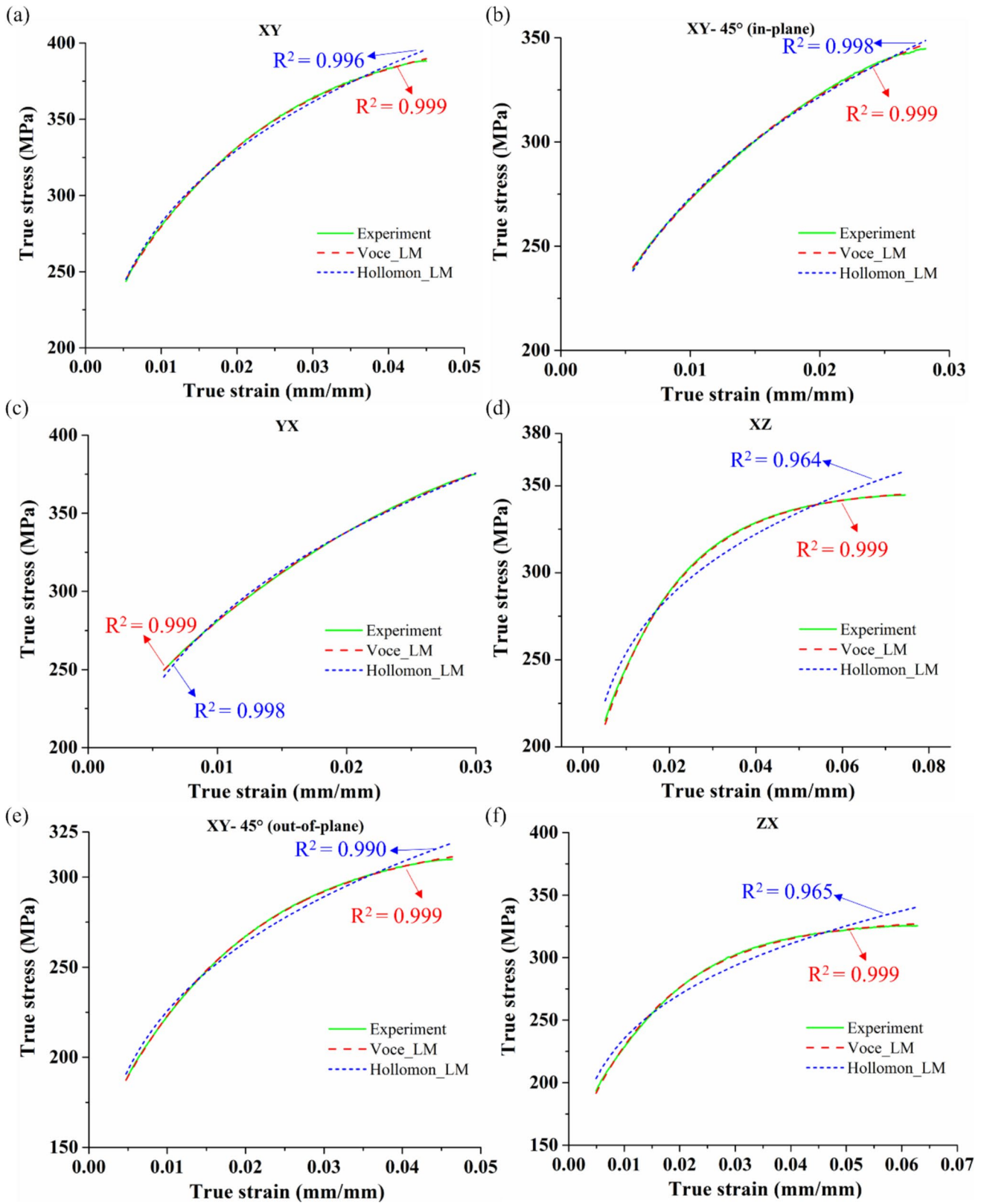


Fig. 5 The Voce and Hollomon approximations obtained from the LM method (Voce_LM and Hollomon_LM) compared with the true stress-true strain curves for **a** XY, **b** XY_{45°} (in-plane), **c** YX, **d** XZ,

e XY_{45°} (out-of-plane), and **f** ZX build orientations. The coefficient of determination (COD), R^2 , is also presented to show the goodness of fit

Table 4 The Hollomon_LM parameters (n_{HLM}, K_{HLM}) and Voce_LM parameters ($\sigma_{S_{LM}}, n_{V_{LM}}, K_{V_{LM}}$) used for work hardening approximation for PBF-LB AlSi10Mg with different heat-treatment and build-orientation conditions

Orientation	Heat treatment	n_{HLM}	K_{HLM} (MPa)	$\sigma_{S_{LM}}$ (MPa)	$n_{V_{LM}}$	$K_{V_{LM}}$	Ref
XY	300 °C/2 h	0.23	795.4	224.90	63.95	394	Current work
XY_45° (in-plane)	300 °C/2 h	0.24	806.9	204.40	55.34	390.10	Current work
YX	300 °C/2 h	0.26	937.0	257.50	40.08	453.40	Current work
XZ	300 °C/2 h	0.17	559.4	177.40	55.23	348.10	Current work
XY_45° (out-of-plane)	300 °C/2 h	0.23	637.4	179.30	57.78	323.60	Current work
ZX	300 °C/2 h	0.20	593	188.80	61.94	345.30	Current work
XZ	170 °C/90 min	0.20	861.44	502.98	249.71	37.85	[5]
XZ	244 °C/180 min	0.22	732.16	384.59	201.37	52.04	[5]
XZ	290 °C/45 min	0.20	615.27	341.31	176.16	56.20	[5]
ZX	170 °C/90 min	0.27	1038.55	467.90	279.81	51.51	[5]
ZX	244 °C/180 min	0.29	929.73	391.49	256.49	56	[5]
ZX	290 °C/45 min	0.26	800.36	362.20	234.02	60.73	[5]
XY	-	0.25	966.33	549.22	320.17	26.93	[10]
XY	300 °C/2 h	0.14	427.95	301.89	135.83	48.04	[10]
XY	530 °C/2 h	0.19	428.21	296.04	148.58	21.86	[10]
XY	-	0.44	2710.40	-	-	-	[20]
XY	300 °C/2 h	0.18	519.31	306.75	154.37	61.167	[20]
XY	530 °C/6 h	0.21	446.88	290.13	155.72	25.044	[20]
ZX	-	0.36	1448.41	619.03	444.32	25.126	[20]
ZX	300 °C/2 h	0.18	518.40	313.45	160.81	57.47	[20]
ZX	530 °C/6 h	0.20	423	281.30	149.62	22.61	[20]
XY	-	0.23	904.10	552.88	309.92	24.26	[34]
ZX	-	0.26	964.07	536.12	352.54	31.36	[34]

in ranges for both H_c ranges of AB and HT samples for PBF-LB AlSi10Mg alloy testes at different strain rates, showing ranges of 0.434–0.641 for AB samples and 0.721–0.876 for HT. Comparing this to the current paper’s ranges, the current works ranges engulf ranges found in [40]. This could be due to the much larger sample size and variation in printing parameters (such as building orientation, layer height, laser power intensity, scanning speed, hatch spacing, powder type, and particle size) for both AB and HT samples, with Ref. [40] only producing 6 samples of varying strain rate for AB and HT ranges.

4.4 Toughness

The toughness, defined as the area under the true stress-true strain curve, was found by solving the integral of the true stress-true strain curve. This integral was solved using the Python code based on a cubic spline interpolation function and then subsequently solved using Simpson’s rule [41]. In doing so, upper and lower values of true strain as inputs, along with the full arrays of both true stress and true strain, are used to produce the full integrated approximation as an output representing the toughness. The toughness was used as a good indicator of the work hardening rate since toughness considers both strength and ductility. Therefore, to have

high toughness, there is a requirement to have both high strength and high ductility. Both properties of strength and ductility are known to be mutually exclusive, meaning that increasing one factor, such as strength, will in turn sacrifice (reduce) the ductility; this is well known as the strength-ductility trade-off [21]. An optimum value of work hardening, therefore, must exist to reach the maximum toughness value [21].

UTS and elongations at fracture are the two parameters involved in determining toughness. Figure 7 shows UTS, elongation at fracture and toughness for different build orientations. The toughness values are $14.2 \text{ MJ} \cdot \text{m}^{-3}$, $7.7 \text{ MJ} \cdot \text{m}^{-3}$, $9.0 \text{ MJ} \cdot \text{m}^{-3}$, $21.4 \text{ MJ} \cdot \text{m}^{-3}$, $11.9 \text{ MJ} \cdot \text{m}^{-3}$ and $18.1 \text{ MJ} \cdot \text{m}^{-3}$ for XY, XY_45° (in-plane), YX, XZ, XY_45° (out-of-plane) and ZX, respectively. As reported in Table 1, the UTS values for XY, XY_45° (in-plane), YX, XZ, XY_45° (out-of-plane), and ZX orientation are 366.60 ± 4.60 , 332.60 ± 4.90 , 349 ± 7 , 327.8 ± 8.60 , 295.80 ± 7.10 , and 306.10 ± 1.40 , respectively. Also, the fracture strain values for XY, XY_45° (in-plane), YX, XZ, XY_45° (out-of-plane), and ZX orientation are 4.70 ± 0.30 , 2.80 , 3 ± 0.20 , 0.57 ± 0.12 , 4.60 ± 0.50 , and 5.90 ± 1.50 , respectively. There is a much larger variation in the elongation at fracture than there is with the UTS between each orientation of AlSi10Mg, meaning that the variation in the toughness

Table 5 Sensitivity analysis results for the Hollomon_LM method showing parameter percentage change, associated R^2 value, and deviation from the original R^2 value for each printing orientation

Orientation	Parameter change	R^2 after applying parameter change	Deviation from baseline R^2
XY	$K_{\text{HLM}} + 5\%$	0.8192	0.1772
	$K_{\text{HLM}} - 5\%$	0.8172	0.1792
	$n_{\text{HLM}} + 5\%$	0.8746	0.1218
	$n_{\text{HLM}} - 5\%$	0.8653	0.1311
XY_45° (in-plane)	$K_{\text{HLM}} + 5\%$	0.7789	0.2191
	$K_{\text{HLM}} - 5\%$	0.7746	0.2234
	$n_{\text{HLM}} + 5\%$	0.7973	0.2007
	$n_{\text{HLM}} - 5\%$	0.7810	0.2170
YX	$K_{\text{HLM}} + 5\%$	0.8137	0.1843
	$K_{\text{HLM}} - 5\%$	0.8137	0.1843
	$n_{\text{HLM}} + 5\%$	0.8047	0.1933
	$n_{\text{HLM}} - 5\%$	0.7828	0.2152
XZ	$K_{\text{HLM}} + 5\%$	0.7697	0.1940
	$K_{\text{HLM}} - 5\%$	0.7884	0.1753
	$n_{\text{HLM}} + 5\%$	0.9087	0.0550
	$n_{\text{HLM}} - 5\%$	0.8943	0.0694
XY_45° (out-of-plane)	$K_{\text{HLM}} + 5\%$	0.7920	0.198
	$K_{\text{HLM}} - 5\%$	0.8002	0.1898
	$n_{\text{HLM}} + 5\%$	0.8617	0.1283
	$n_{\text{HLM}} - 5\%$	0.8473	0.1427
ZX	$K_{\text{HLM}} + 5\%$	0.7930	0.1720
	$K_{\text{HLM}} - 5\%$	0.7879	0.1771
	$n_{\text{HLM}} + 5\%$	0.8778	0.0872
	$n_{\text{HLM}} - 5\%$	0.8765	0.0885

values will be dominated by the difference in elongation at fracture. This aligns with the toughness values, with the XZ orientation achieving the highest toughness value as well as the largest elongation at fracture value yet the orientation fails to achieve the highest UTS value out of all the samples. Dong et al. [21] presented a similar trend with the elongation at fracture being the deciding factor for adequate toughness for AlSi10Mg but showed drastically larger toughness value due to the higher ductility imposed by the heat-treatment. They showed that the AB samples producing a toughness value of $24.13 \text{ MJ} \cdot \text{m}^{-3}$, a slightly higher toughness value than the current work deriving mainly from the higher associated elongation shown in the paper.

Although the samples showing the highest strength value may be considered more optimal for a given use case, the decrease in ductility may be undesirable, and therefore, considering toughness will be the most vital property to use when both strength and ductility is necessary. In the case of AlSi10Mg, the orientation in the XZ direction would therefore be the most desirable for achieving the highest toughness value.

Comparing the UTS of the XZ and XY_45° (in-plane) ($327.80 \pm 8.6 \text{ MPa}$ and $332.60 \pm 4.9 \text{ MPa}$ respectively), both samples show similar UTS values yet have an elongation at fracture value of $7.20 \pm 1.1\%$ and 2.8% leading to the large difference in toughness values of $21.4 \text{ MJ} \cdot \text{m}^{-3}$ and $7.7 \text{ MJ} \cdot \text{m}^{-3}$, respectively. Additionally comparing YX samples (UTS of $349.0 \pm 7.0 \text{ MPa}$ and elongation at fracture of $3.00 \pm 0.2\%$) gives a slightly higher toughness value than the XY_45° (in-plane) sample due to the increase in the UTS value. XZ samples (UTS of $327.8 \pm 8.6 \text{ MPa}$ and elongation at fracture of $7.20 \pm 1.1\%$) show a large increase in toughness of all three of the previously mentioned orientations due to the drastic increase in the elongation at fracture. XY_45 (out-of-plane) samples (UTS of $295.80 \pm 7.1 \text{ MPa}$ and elongation at fracture of $4.60 \pm 0.5\%$) shows a decrease in toughness in comparison to XZ due to the large decrease in the elongation at fracture value. ZX sample (UTS of $306.10 \pm 1.4 \text{ MPa}$ and elongation at fracture of $5.90 \pm 1.5\%$) shows the second highest toughness value of all orientations due to the corresponding second highest elongation at fracture value.

Table 6 Sensitivity analysis results for the Voce_LM method showing parameter percentage change, associated R^2 value, and deviation from the original R^2 value for each printing orientation

Orientation	Parameter change	R^2 after applying parameter change	Deviation from baseline R^2
XY	$\sigma_{S_{LM}} + 5\%$	0.8088	0.1902
	$\sigma_{S_{LM}} - 5\%$	0.6973	0.3017
	$K_{V_{LM}} + 5\%$	0.9775	0.0215
	$K_{V_{LM}} - 5\%$	0.9904	0.0086
	$n_{V_{LM}} + 5\%$	0.9917	0.0073
	$n_{V_{LM}} - 5\%$	0.9772	0.0218
XY_45° (in-plane)	$\sigma_{S_{LM}} + 5\%$	0.6313	0.3682
	$\sigma_{S_{LM}} - 5\%$	0.6357	0.3638
	$K_{V_{LM}} + 5\%$	0.9793	0.0202
	$K_{V_{LM}} - 5\%$	0.9776	0.0219
	$n_{V_{LM}} + 5\%$	0.9884	0.0111
	$n_{V_{LM}} - 5\%$	0.9877	0.0118
YX	$\sigma_{S_{LM}} + 5\%$	0.6401	0.3597
	$\sigma_{S_{LM}} - 5\%$	0.6400	0.3598
	$K_{V_{LM}} + 5\%$	0.9675	0.0323
	$K_{V_{LM}} - 5\%$	0.9675	0.0323
	$n_{V_{LM}} + 5\%$	0.9879	0.0119
	$n_{V_{LM}} - 5\%$	0.9869	0.0129
XZ	$\sigma_{S_{LM}} + 5\%$	0.8499	0.1491
	$\sigma_{S_{LM}} - 5\%$	0.6262	0.3728
	$K_{V_{LM}} + 5\%$	0.9496	0.0494
	$K_{V_{LM}} - 5\%$	0.9887	0.0103
	$n_{V_{LM}} + 5\%$	0.9902	0.0088
	$n_{V_{LM}} - 5\%$	0.9522	0.0468
XY_45° (out-of-plane)	$\sigma_{S_{LM}} + 5\%$	0.7417	0.2581
	$\sigma_{S_{LM}} - 5\%$	0.7336	0.2662
	$K_{V_{LM}} + 5\%$	0.9903	0.0095
	$K_{V_{LM}} - 5\%$	0.9918	0.0080
	$n_{V_{LM}} + 5\%$	0.9935	0.0063
	$n_{V_{LM}} - 5\%$	0.9908	0.009
ZX	$\sigma_{S_{LM}} + 5\%$	0.7786	0.2209
	$\sigma_{S_{LM}} - 5\%$	0.7798	0.2197
	$K_{V_{LM}} + 5\%$	0.9939	0.0056
	$K_{V_{LM}} - 5\%$	0.9935	0.0060
	$n_{V_{LM}} + 5\%$	0.9945	0.0050
	$n_{V_{LM}} - 5\%$	0.9940	0.0055

Overall, this comparison shows the significant effect that elongation at fracture has on the toughness value.

In summary, this section investigated the effect of build orientation on the toughness of AlSi10Mg, showing that toughness is primarily influenced by elongation at fracture rather than UTS. The XZ orientation exhibited the highest toughness ($21.4 \text{ MJ}\cdot\text{m}^{-3}$) due to its superior elongation at fracture, highlighting the importance of balancing strength and ductility for optimal material performance.

4.5 Estimating Vickers hardness using tensile testing, without performing hardness test

Utilising Eq. 6, with knowledge of H_v and σ_Y , an estimation of the work hardening exponent n_H can be obtained. Alternatively, utilising n_H from the Hollomon approximation and σ_Y , an estimation of H_v can be achieved. This is extremely beneficial as it allows one to only perform tensile testing to determine the Vickers hardness of a given AM material,

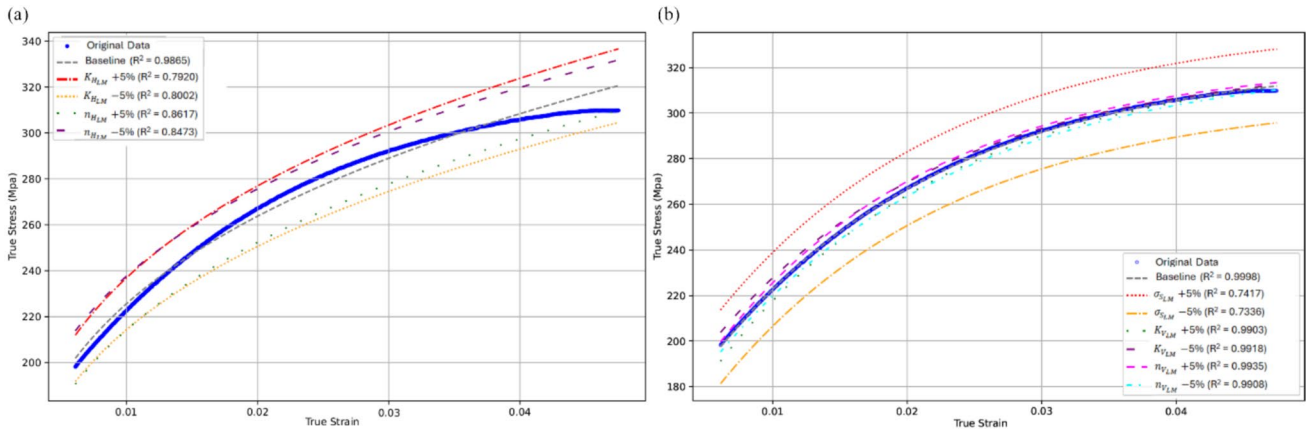
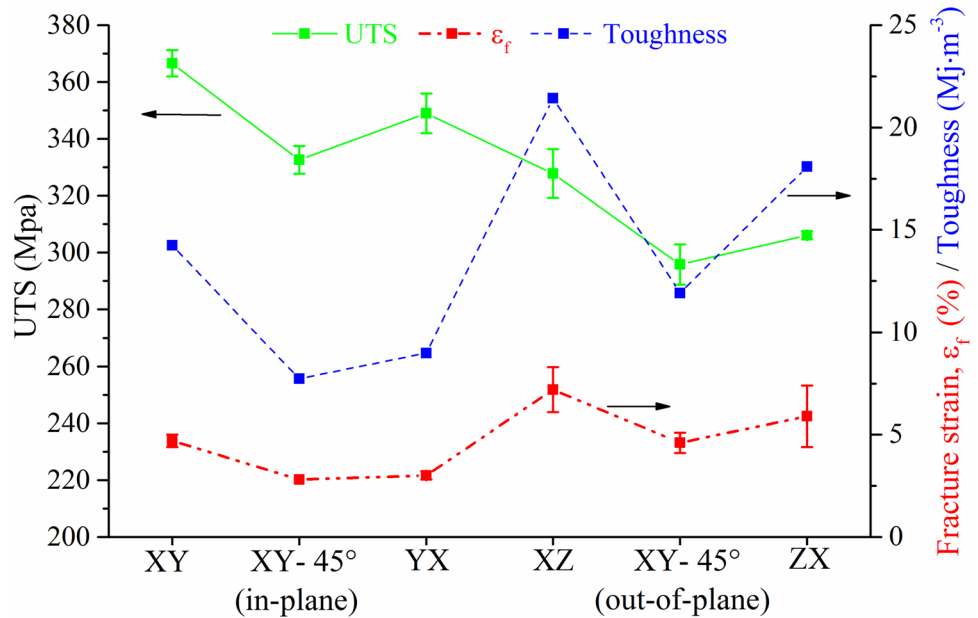


Fig. 6 Representative sensitivity analyses of a Hollomon_LM and b Voce_LM, for the sample with XY_45° (out-of-plane) orientation

Fig. 7 UTS, elongation at fracture (%) and toughness for different build orientations



without a need for performing hardness testing specially in the absence of hardness testing facilities. Using Eq. 7 with σ_u and n_H as inputs will also allow to find an estimation of H_v purely through tensile testing. Table 7 gives the Vickers hardness, obtained from experimental measurements, and Eqs. 6 and 7, for samples printed at different orientations. The n_H form original Hollomon method, $n_{Horiginal}$ (see Table 2), and n_H form Hollomon_LM method, n_{HLM} (see Table 4), were used in Eqs. 6 and 7 to estimate the Vickers hardness. The errors in Table 7 for values obtained using Eqs. 6 and 7 were calculated using upper and lower ranges for UTS and YS (from Table 1), respectively. The results are also compared in Fig. 8.

Equations 6 and 7 with $n_{Horiginal}$ and n_{HLM} as an input to estimate hardness values for samples printed at different

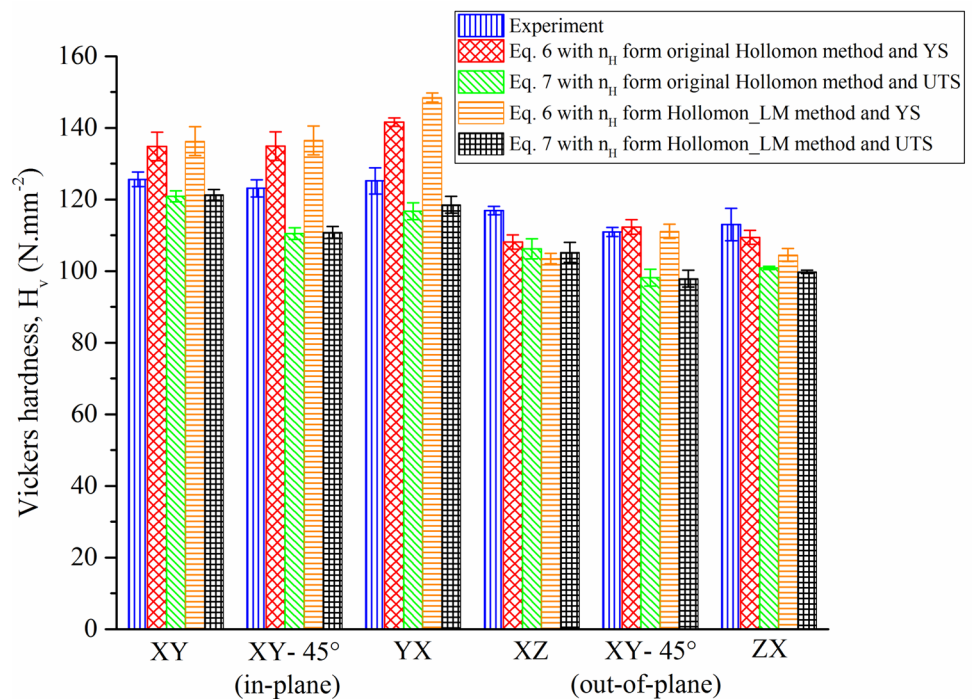
orientations provided different levels of accuracy. For example, Eq. 6 with n_{HLM} as the input, overestimated the hardness values for XY, XY_45° (in-plane), and YX specimens. For the XZ specimen, Eq. 6 with n_{HLM} underestimated hardness value slightly more than Eq. 6 using $n_{Horiginal}$. Equation 7 with n_{HLM} as an input provided a slightly more accurate estimation of the experimental hardness values for XY, XY_45° (in-plane), and YX samples compared to Eq. 7 with $n_{Horiginal}$ as an input. Equation 7 with $n_{Horiginal}$ as an input gave slightly more accurate estimation of hardness values for the XZ, XY_45° (out-of-plane), and ZX orientations in comparison to Eq. 7 with n_{HLM} as an input.

Accurate determination n_H is critical in the proposed method. A potential source of error with this method is the utilisation of n_H from the work hardening curve as

Table 7 Vickers hardness, obtained from experimental measurements, and Eqs. 6 and 7 using YS, UTS, n_H form original Hollomon method ($n_{Horiginal}$) and n_H form Hollomon_LM method (n_{HLM}) for samples printed at different orientations

Orientation	Hardness				
	$H_v(N.mm^{-2})$ from experiment	$H_v(N.mm^{-2})$ using $n_{Horiginal}$ and YS in Eq. 6	$H_v(N.mm^{-2})$ using n_{HLM} and YS in Eq. 6	$H_v(N.mm^{-2})$ using $n_{Horiginal}$ and UTS in Eq. 7	$H_v(N.mm^{-2})$ using n_{HLM} and UTS in Eq. 7
XY	125.60 ± 2.03	134.80 ± 3.98	136.30 ± 4.03	120.90 ± 1.52	121.30 ± 1.52
XY_45° (in-plane)	123.10 ± 2.36	134.90 ± 3.96	136.50 ± 4.01	110.5 ± 1.63	110.80 ± 1.63
YX	125.20 ± 3.65	141.60 ± 1.21	148.50 ± 1.28	116.70 ± 2.34	118.50 ± 2.34
XZ	116.90 ± 1.2	108.10 ± 2.01	103.50 ± 1.43	106.20 ± 2.79	105.20 ± 2.79
XY_45° (out-of-plane)	110.90 ± 1.25	112.30 ± 2.04	111.10 ± 2.02	98.20 ± 2.36	97.90 ± 2.36
ZX	113 ± 4.50	109.40 ± 1.94	104.50 ± 1.85	100.90 ± 0.46	99.80 ± 0.46

Fig. 8 Comparison of Vickers hardness experimental measurements [7] with those obtained using Eqs. 6 and 7



well as using YS and UTS values and each one of these parameters, once found experimentally from tensile tests, have their own error (standard deviation (SD)). Therefore, using these parameters to estimate another parameter (in this case Vickers hardness) will magnify errors, and hence, it should be noted that Eqs. 6 and 7 are proposed for materials processed through constrained groove pressing method [28] and not for AM materials with anisotropic properties. Nonetheless, using these equations here for AM materials were investigated, and it was shown that, given their limitations, they gave close estimation of hardness measurements.

5 Conclusions and future work

This paper investigates various mechanical properties derived from tensile testing, including toughness, hardening capacity, yield strength, UTS, and elongation at fracture for each alloy and for multiple printing orientations. The key findings are as follows:

- (I) Toughness and UTS variation:
 - Toughness values for AlSi10Mg showed a similar trend to UTS across multiple printing orientations.

- The significant variation in toughness values was primarily attributed to the large differences in elongation at fracture observed in different orientations.
- (II) Hardening capacity in as-built (AB) and heat-treated (HT) samples:
- The hardening capacity ranges for as-built (AB) and heat-treated (HT) samples showed a close resemblance, which can be attributed to the wide variation in printing parameters used for both conditions.
- (III) Comparison of Voce and Hollomon parameters:
- A comprehensive comparison of the original Voce and Hollomon parameter ranges for AB and HT samples revealed that the high variability in HT samples was due to the diverse thermal treatments reported in the literature.
 - These variances in thermal treatments significantly impacted the stress–strain curves and, consequently, the Voce and Hollomon parameters.
- (IV) Levenberg–Marquardt (LM) method for improved accuracy:
- One of the novelties of the current paper is presenting the underlying superiority in the LM least square method over the original method.
 - The LM method used to find parameters for Hollomon or Voce approximations is found to provide superior approximation accuracy compared to the original Hollomon and Voce methods, giving higher R² values for all building orientations.
 - Voce_LM is shown to be the superior approximation method in terms of accuracy over the Hollomon_LM. This is likely due to the Hollomon approximation providing an overestimation of the experimental data at higher strains.
- (V) New Vickers hardness estimation method:
- This study proposes a novel approach for estimating the Vickers hardness for a given AM metal, utilising UTS or *YS* coupled with work hardening exponent, n_H , from original Hollomon or Hollomon_LM methods.
 - This method enables hardness estimation purely from tensile testing, potentially reducing both the time and cost associated with hardness testing, especially when hardness testing facilities are unavailable.

Although the method of estimating Vickers hardness from parameters derived from the stress–strain curve showed potential in estimating Vickers hardness, however,

Eqs. 6 and 7 were not tailored to PBF-LB alloys. The parameters of 3 and 2.9 from Eqs. 6 and 7 are tailored to casting alloys originally. Therefore, future work should explore new such parameters for both equations. Additionally, due to the complex printing method of PBF-LB, each sample produces different results based on many factors such as heat treatment, applied loading strain rate, and temperature. Modifying Eqs. 6 and 7 to account for these parameters could also increase the accuracy of the approximation. Furthermore, the applicability of this hardness prediction model to other material systems depends on their deformation mechanisms and microstructural characteristics. Future work should focus on extending this model by incorporating material-specific correction factors or developing alternative formulations better suited to anisotropic AM materials. Furthermore, since this paper focused only on a comparison between Voce and Hollomon equations, a comprehensive comparison between other approximations such as Kock-Mecking [42] or Swift [43] equations with application for estimating work hardening of AM materials should be explored in future work.

Appendix. Levenberg–Marquardt (LM) algorithm

The Levenberg–Marquardt (LM) algorithm is used for solving nonlinear least square problems. The algorithm consists of defining the function, initializing parameters in the function, and creating an iteration loop that actively adjusts the parameters to minimise the objective function. The formula used combines the aspects of the Gauss–Newton method and the steepest descent method. The general form of the LM algorithm is as follows [44]:

$$(J^T J + \lambda I) \delta = J^T [y - f(\beta)] \quad (A1)$$

where J is the Jacobian matrix, with row i being J_i and $f(\beta)$, and y is a vector with $f(X_i, \beta)$ and y_i as much as I , and δ is the value that gives the change in direction in the calculation of the vector parameter. Derived from the gradient descent method, λ serves as the damping parameter. It is always a positive value and is adjusted for each iteration. Shastry et al. [24] used the LM algorithm to predict the work hardening proportion of the stress–strain curve for 2.25 Cr-1Mo steel and has success in presenting the validity of the method for the Voce equation.

Data availability Data will be made available on request.

Declarations

Conflict of interest The authors declare no competing interests.

Open Access This article is licensed under a Creative Commons Attribution 4.0 International License, which permits use, sharing, adaptation, distribution and reproduction in any medium or format, as long as you give appropriate credit to the original author(s) and the source, provide a link to the Creative Commons licence, and indicate if changes were made. The images or other third party material in this article are included in the article's Creative Commons licence, unless indicated otherwise in a credit line to the material. If material is not included in the article's Creative Commons licence and your intended use is not permitted by statutory regulation or exceeds the permitted use, you will need to obtain permission directly from the copyright holder. To view a copy of this licence, visit <http://creativecommons.org/licenses/by/4.0/>.

References

- Song L, Yuan S, Zhao L, Zhu Y, Liang S, Huang M, Simar A, Li Z (2023) Deciphering phase stress partition and its correlation to mechanical anisotropy of laser powder bed fusion AlSi10Mg. *Addit Manuf* 71:103594. <https://doi.org/10.1016/j.addma.2023.103594>
- Yi D, Li T, Zhang D, Liu Z, Wei Y, Li X (2024) Particulate-reinforced AlSi10Mg matrix composites fabricated by laser powder bed fusion: a review. *J Manuf Process* 132:912–934. <https://doi.org/10.1016/j.jmapro.2024.11.011>
- Sheng X, Guo A, Guo S, Sui S, Yang W, Tang R, Li X, Qu P, Wang M, Lin X (2024) Laser powder bed fusion for the fabrication of triply periodic minimal surface lattice structures: synergistic macroscopic and microscopic optimization. *J Manuf Process* 119:179–192. <https://doi.org/10.1016/j.jmapro.2024.03.081>
- Yang W, Guo A, Sheng X, Tang R, Qu P, Wang S, Liu C, Yin L, Sui S, Guo S (2025) Preparation of 316L stainless steel/WC gradient layered structures with excellent strength-elongation synergy using laser powder bed fusion. *J Manuf Process* 133:692–704. <https://doi.org/10.1016/j.jmapro.2024.11.093>
- Fiocchi J, Biffi CA, Colombo C, Vergani LM, Tuissi A (2020) Ad hoc heat treatments for selective laser melted AlSi10Mg alloy aimed at stress-relieving and enhancing mechanical performances. *JOM* 72(3):1118–1127. <https://doi.org/10.1007/s11837-019-03973-z>
- Chen B, Moon SK, Yao X, Bi G, Shen J, Umeda J, Kondoh K (2017) Strength and strain hardening of a selective laser melted AlSi10Mg alloy. *Scr Mater* 141:45–49. <https://doi.org/10.1016/j.scriptamat.2017.07.025>
- Song L, Zhao L, Ding L, Zhu Y, Huang M, Simar A, Li Z (2022) Microstructure and loading direction dependent hardening and damage behavior of laser powder bed fusion AlSi10Mg. *Mater Sci Eng A* 832:142484. <https://doi.org/10.1016/j.msea.2021.142484>
- Van Cauwenbergh P, Samaee V, Thijs L, Nejezchlebová J, Sedláč P, Iveković A, Schryvers D, Van Hooreweder B, Vanmeensel K (2021) Unravelling the multi-scale structure–property relationship of laser powder bed fusion processed and heat-treated AlSi10Mg. *Sci Rep* 11(1):6423. <https://doi.org/10.1038/s41598-021-85047-2>
- Bao J, Wu Z, Wu S, Hu D, Sun W, Wang R (2022) The role of defects on tensile deformation and fracture mechanisms of AM AlSi10Mg alloy at room temperature and 250 °C. *Eng Fract Mech* 261:108215. <https://doi.org/10.1016/j.engfracmech.2021.108215>
- Takata N, Liu M, Kodaira H, Suzuki A, Kobashi M (2020) Anomalous strengthening by supersaturated solid solutions of selectively laser melted Al–Si-based alloys. *Addit Manuf* 33:101152. <https://doi.org/10.1016/j.addma.2020.101152>
- Zhao L, Song L, Santos Macías JG, Zhu Y, Huang M, Simar A, Li Z (2022) Review on the correlation between microstructure and mechanical performance for laser powder bed fusion AlSi10Mg. *Addit Manuf* 56:102914. <https://doi.org/10.1016/j.addma.2022.102914>
- Li X, Yi D, Wu X, Zhang J, Yang X, Zhao Z, Feng Y, Wang J, Bai P, Liu B et al (2021) Effect of construction angles on microstructure and mechanical properties of AlSi10Mg alloy fabricated by selective laser melting. *J Alloys Compd* 881:160459. <https://doi.org/10.1016/j.jallcom.2021.160459>
- Zhang XX, Lutz A, Andrä H, Lahres M, Gong W, Harjo S, Emmelmann C (2022) Strain hardening behavior of additively manufactured and annealed AlSi3.5Mg2.5 alloy. *J Alloys Compd* 898:162890. <https://doi.org/10.1016/j.jallcom.2021.162890>
- Estrin Y, Mecking H (1984) A unified phenomenological description of work hardening and creep based on one-parameter models. *Acta Metall* 32(1):57–70. [https://doi.org/10.1016/0001-6160\(84\)90202-5](https://doi.org/10.1016/0001-6160(84)90202-5)
- Ming X, Song D, Yu A, Tan H, Zhang Q, Zhang Z, Chen J, Lin X (2023) Effect of heat treatment on microstructure, mechanical and thermal properties of selective laser melted AlSi7Mg alloy. *J Alloys Compd* 945:169278. <https://doi.org/10.1016/j.jallcom.2023.169278>
- Konda Gokuldoss P (2019) Work Hardening in selective laser melted Al-12Si alloy. *Mater Des Process Commun* 1(2):e46. <https://doi.org/10.1002/mdp2.46>
- Baxter C, Cyr E, Odeshi A, Mohammadi M (2018) Constitutive models for the dynamic behaviour of direct metal laser sintered AlSi10Mg_200C under high strain rate shock loading. *Mater Sci Eng A* 731:296–308. <https://doi.org/10.1016/j.msea.2018.06.040>
- Clyne TW, Campbell JE (2021) Testing of the plastic deformation of metals. Cambridge University Press. <https://doi.org/10.1017/9781108943369>
- Lupi G, Minerva G, Patriarca L, Casati R, Beretta S (2024) Fracture toughness of AlSi10Mg alloy produced by LPBF: effects of orientation and heat treatment. *Int J Fract* 247(3):329–344. <https://doi.org/10.1007/s10704-024-00787-2>
- Takata N, Kodaira H, Sekizawa K, Suzuki A, Kobashi M (2017) Change in microstructure of selectively laser melted AlSi10Mg alloy with heat treatments. *Mater Sci Eng A* 704:218–228. <https://doi.org/10.1016/j.msea.2017.08.029>
- Dong XX, Shen YF, Zhu YT (2023) Moderating strain hardening rate to produce high ductility and high strength in a medium carbon TRIP steel. *Mater Res Lett* 11(1):69–75. <https://doi.org/10.1080/21663831.2022.2116295>
- Wan J, Chen B, Shen J, Kondoh K, Liu S, Li J (2024) Improving the mechanical properties of laser powder bed fused AlSi10Mg alloys by eliminating the inevitable micro-voids via hot forging. *Rapid Prototyp J* 30(4):621–632. <https://doi.org/10.1108/RPJ-06-2023-0202>
- Tang H, Gao C, Zhang Y, Zhang N, Lei C, Bi Y, Tang P, Rao JH (2023) Effects of direct aging treatment on microstructure, mechanical properties and residual stress of selective laser melted AlSi10Mg alloy. *J Mater Sci Technol* 139:198–209. <https://doi.org/10.1016/j.jmst.2022.08.032>
- Shastri CG, Mathew MD, BhanuSankara Rao K, Mannan SL (2004) Analysis of elevated temperature flow and work hardening behaviour of service-exposed 2.25Cr-1Mo steel using Voce equation. *Int J Press Vessel Pip* 81(3):297–301. <https://doi.org/10.1016/j.ijpvp.2003.11.016>
- Estrada-Ruiz RH, Flores-Campos R, Herrera-Ramírez JM, Muñoz-Andrade JD, Martínez-Sánchez R (2022) Tensile flow behavior of AA7075–Ag/C composites evaluated by the Hollomon and Voce equations. *Adv Powder Technol* 33(12):103873. <https://doi.org/10.1016/j.apt.2022.103873>
- Kocks F (1976) Laws for work-hardening and low-temperature creep. *J Eng Mater Technol* 98:76–85. <https://doi.org/10.1115/1.3443340>

27. Southern TJF, Campbell JE, Fang C, Nemcova A, Bannister A, Clyne TW (2023) Use of hardness, PIP and tensile testing to obtain stress-strain relationships for metals. *Mech Mater* 187:104846. <https://doi.org/10.1016/j.mechmat.2023.104846>
28. Khodabakhshi F, Haghshenas M, Eskandari H, Koohbor B (2015) Hardness-strength relationships in fine and ultra-fine grained metals processed through constrained groove pressing. *Mater Sci Eng A* 636:331–339. <https://doi.org/10.1016/j.msea.2015.03.122>
29. Serjouei A, Libura T, Brodecki A, Radziejewska J, Broniszewska P, Pawłowski P, Szymczak T, Bodaghi M, Kowalewski ZL (2022) Strength-hardness relationship for AlSi10Mg alloy produced by laser powder bed fusion: an experimental study. *Mater Sci Eng A* 861:144345. <https://doi.org/10.1016/j.msea.2022.144345>
30. ISO 6507-1: (2018) Metallic materials — Vickers hardness test — part 1: test method. International Organization for Standardization, Geneva, Switzerland
31. Liu F, Chen Y, He C, Li L, Wang C, Li H, Zhang H, Wang Q, Liu Y (2021) Tensile and very high cycle fatigue behaviors of a compressor blade titanium alloy at room and high temperatures. *Mater Sci Eng A* 811:141049. <https://doi.org/10.1016/j.msea.2021.141049>
32. Saltelli A, Ratto M, Andres T, Campolongo F, Cariboni J, Gatelli D, Saisana M, Tarantola S (2008) *Global sensitivity analysis: the primer*. Wiley, LTD, Chichester
33. Rosenthal I, Stern A, Frage N (2017) Strain rate sensitivity and fracture mechanism of AlSi10Mg parts produced by selective laser melting. *Mater Sci Eng A* 682:509–517. <https://doi.org/10.1016/j.msea.2016.11.070>
34. Zhao L, Santos Macías JG, Douillard T, Li Z, Simar A (2021) Unveiling damage sites and fracture path in laser powder bed fusion AlSi10Mg: comparison between horizontal and vertical loading directions. *Mater Sci Eng A* 807:140845. <https://doi.org/10.1016/j.msea.2021.140845>
35. Awd M, Tenkamp J, Hirtler M, Siddique S, Bambach M, Walther F (2018) Comparison of microstructure and mechanical properties of Scalmalloy® produced by selective laser melting and laser metal deposition. *Materials*. <https://doi.org/10.3390/ma11010017>
36. Fite J, EswarappaPrameela S, Slotwinski J, Weihs TP (2023) Enhanced mechanical properties by eutectic cells in AlSi10Mg - a promising paradigm for strengthening aluminum in additive manufacturing. *Mater Charact* 204:113179. <https://doi.org/10.1016/j.matchar.2023.113179>
37. Tsuji N, Kamikawa N, Ueji R, Takata N, Koyama H, Terada D (2008) Managing both strength and ductility in ultrafine grained steels. *ISIJ Int* 48(8):1114–1121. <https://doi.org/10.2355/isijinternational.48.1114>
38. Fang S, Zheng X, Guo B, Sia B, Yang L (2023) A new method for localized necking detection in uniaxial tensile testing based on a multi-camera DIC system. *Mater Today Commun* 35:106021. <https://doi.org/10.1016/j.mtcomm.2023.106021>
39. Zhou L, Mehta A, Schulz E, McWilliams B, Cho K, Sohn Y (2018) Microstructure, precipitates and hardness of selectively laser melted AlSi10Mg alloy before and after heat treatment. *Mater Charact* 143:5–17. <https://doi.org/10.1016/j.matchar.2018.04.022>
40. Wang X, Nan X, Ma C, Shi T, Guo M, Hu J, Wang Y (2024) Strain rate dependence of mechanical behavior in an AlSi10Mg alloy with different states fabricated by laser powder bed fusion. *J Mater Res Technol* 32:1354–1367. <https://doi.org/10.1016/j.jmrt.2024.08.006>
41. Kareem HJ, Abdulwahid MA, Hasini H (2023) Experimental investigation of holdup fraction using the trapezoidal rule, simpson's rule and the average offset formula in perforated horizontal wellbore. *Results Eng* 18:101131. <https://doi.org/10.1016/j.rineng.2023.101131>
42. Zhang Z, Qu Z, Xu L, Liu R, Zhang P, Zhang Z, Langdon TG (2022) A general physics-based hardening law for single phase metals. *Acta Mater* 231:117877. <https://doi.org/10.1016/j.actamat.2022.117877>
43. Prasad K, Kumar D, Krishnaswamy H, Banerjee DK (2023) Uncertainties in the Swift hardening law parameters and their influence on the flow stress and the hole expansion behavior of dual-phase (DP600) steel specimens. *J Mater Eng Perform* 32(20):9206–9220. <https://doi.org/10.1007/s11665-022-07793-2>
44. Aryatama FY, Kurniadi FI, Manik NI (2023) Mathematical model estimation and prediction application of Covid-19 infection in Indonesia using Levenberg-Marquardt algorithm based on Python. *Procedia Comput Sci* 216:120–127. <https://doi.org/10.1016/j.procs.2022.12.118>

Publisher's Note Springer Nature remains neutral with regard to jurisdictional claims in published maps and institutional affiliations.